Chapter 13

Digital Holographic Interferometry for Analysing High-Density Gradients in Fluid Mechanics

Jean-Michel Desse and François Olchewsky

Additional information is available at the end of the chapter

http://dx.doi.org/10.5772/66111

Abstract

Digital holographic interferometry has been developed by ONERA for analysing high refractive index variations encountered in fluid mechanics. First, the authors present the analysis of a small supersonic jet using three different optical techniques based on digital Michelson holography, digital holography using Wollaston prisms and digital holography without reference wave. A comparison of the three methods is given. Then, two different interferometers are described for analysing high-density gradients encountered in high subsonic and transonic flows. The time evolution of the gas density field around a circular cylinder is given at Mach 0.7. Finally, a digital holographic method is presented to visualize and measure the refractive index variations occurring inside a transparent and strongly refracting object. For this case, a comparison with digital and image holographic interferometry using transmission and reflection holograms is provided.

Keywords: digital holography, holographic interferometry, real-time holography, phase measurement

1. Introduction

In-line and off-axis digital holographic interferometry is now became an optical metrological tool more and more used in the domain of fluid mechanics [1]. For instance, it is widely developed in macro- or microscopy for measuring in the flow the location or size of particles [2, 3] or for measuring the temperature or the thermal exchanges in the flames [4, 5]. Other authors have developed digital colour holographic interferometry by using three different wavelengths (one red, one green and one blue) as a luminous source. Qualitative results have

been obtained for visualizing convective flows induced by the thermal dissipation in a tank filled with oil [6]. Quantitatively, the feasibility of three-wavelength digital holographic interferometry has been demonstrated for analysing the variations in the refractive index induced by a candle flame [7] and the technique has been applied in wind tunnel on two-dimensional unsteady flows where the time evolution of the gas density field has been determined on the subsonic near wake flow downstream a circular cylinder [8]. But, when the flow regime reaches the transonic or supersonic domain, problems appear because refractive index gradients become very strong and a shadow effect is generated by the shock waves, for instance, superimposes to the micro-fringes of interferences. Phase shifts appear and limit the interferogram analysis. In order to solve these different problems, the authors propose to study three different cases of flows presenting high-density gradients using specific optical techniques based on digital holography. The first one concerns a small supersonic jet analysed by Michelson colour digital interferometry, colour holographic interferometry using Wollaston prisms and monochromatic digital holography without reference wave. The second case is to compare Michelson and Mach-Zehnder interferometers for analysing the unsteady wake flow around a circular cylinder at transonic Mach number. And finally, digital and image holographic methods are presented to visualize and measure the refractive index variations, convection currents or thermal gradients occurring inside a transparent and strongly refracting object. In the case of image holographic interferometry, a comparison with transmission and reflection holograms is provided.

2. Fundamental

Digital holography has been widely developed for analysing diffusive objects since the digitally reconstructing of the optical wavefront was shown by Goodman and Lawrence [9]. But, in fluid mechanics, the objects under analysis are very often transparent because it is the field of refractive index of the flow which is measured. There are two ways to measure variations in the refractive index by digital holography. The first one, presented in **Figure 1**, is comparable to the technique used for measuring diffusive objects in structural mechanics.

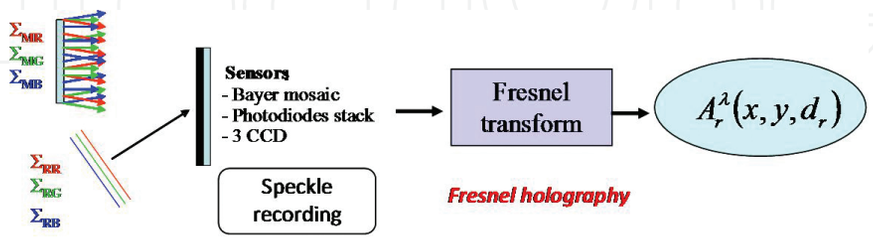

Figure 1. Fresnel holography for measuring transparent objects.

For example, if three different wavelengths are considered, ∑MR for the red line, ∑MG for the green line and ∑MB for the blue line, the wavefronts of measurement which cross the transparent object in the test section can be sent on a ground plate and each point of the plate diffracts

http://dx.doi.org/10.5772/66111

and interferes on the sensor with the three reference waves, ∑RR, ∑RG and ∑RB. In this case, the sensor can be a Bayer mosaic, a stack of photodiodes or a 3CDD. The recorded image is a speckle image which can be processed using Fresnel transform and the field $A_r^{\lambda}(x, y, d_r)$ diffracted at the distance d_r and at the coordinates (x, y) of the observation plane is given by the propagation of the three object waves to the recording plane. The second technique is shown in **Figure 2**. The three wavelengths ∑MR, ∑MG and ∑MB interfere directly onto the sensor with the three reference waves, ∑RR, ∑RG and ∑RB. As the three measurement waves are smooth waves, the interferences with the three reference waves on the sensor produce three gratings of interference micro-fringes which can be used as spatial carrier frequencies, one for each wavelength. By using direct and inverse 2D Fast Fourier Transform (FFT), the amplitude and the phase of the analysed field is obtained.

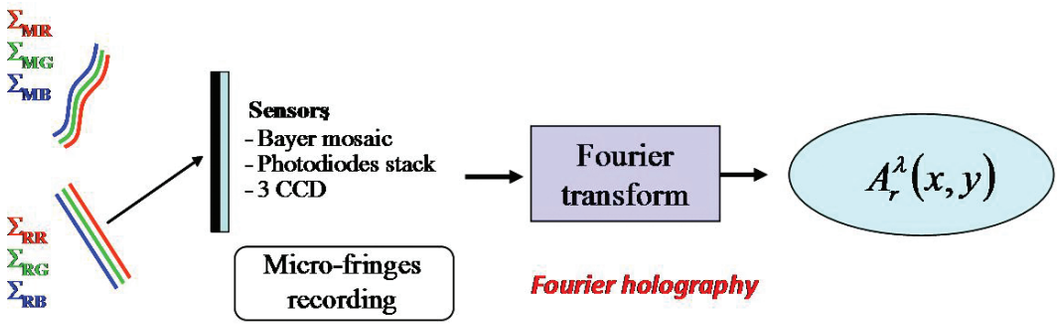

Figure 2. Fourier holography for measuring transparent objects.

All details and basic fundamentals of these two techniques can be found in the study of Picart et al. [10].

3. Digital holography for analysing supersonic jet

In this part, the supersonic flow of a small vertical jet has been analysed using three different techniques based on digital holography. The first one is based on Michelson digital holographic interferometer using three wavelengths as a luminous source [8], the second one uses the same source (three wavelengths) and Wollaston prisms to separate the reference waves and the measurement waves [11] and the last one is a little bit particular because a specific diffraction grating is manufactured to obtain several different diffractions of measurement waves and to avoid having the reference wave [12].

3.1. Michelson holographic interferometry

The optical set-up presented in **Figure 3** is very simple and looks like a conventional Michelson interferometer in which a beam splitter cube (7) is inserted between the spatial filter (6) and the aerodynamic phenomenon under analysis (11). The light source consists of three diode-

pumped solid-state lasers, one red (R), one green (G) and one blue (B), emitting respectively at 660, 532 and 457 nm. A half wave plate (1) is used to rotate by 90° the polarization of the blue line (S to P) and a flat mirror (2) and two dichroic plates (3) allow the superimposing of the three wavelengths. An acousto-optical cell (4) deflects the parasitic wavelengths in a mask (5) and diffracts the three wavelengths RGB using three characteristic frequencies injected into the crystal. The spatial filter (6), composed of microscope objective (60×) and a small hole of 25 μm, is placed at the focal length of the achromatic lens (9) in order to illuminate the phenomenon with a parallel beam. On-going, 50% of the light is returned towards the concave mirror (8) to form the three reference beams and 50% of the light passes through the test section (between (9) and (12) to form the measuring waves. The flat mirror (12) placed behind the test section (11) returns the beams in the beam splitter cube (7). 25% of the light focused on the diaphragm which is placed in front of the achromatic lens (13). It is the same for the 25% of the reference beam which is focused on the same diaphragm by the concave mirror (8).

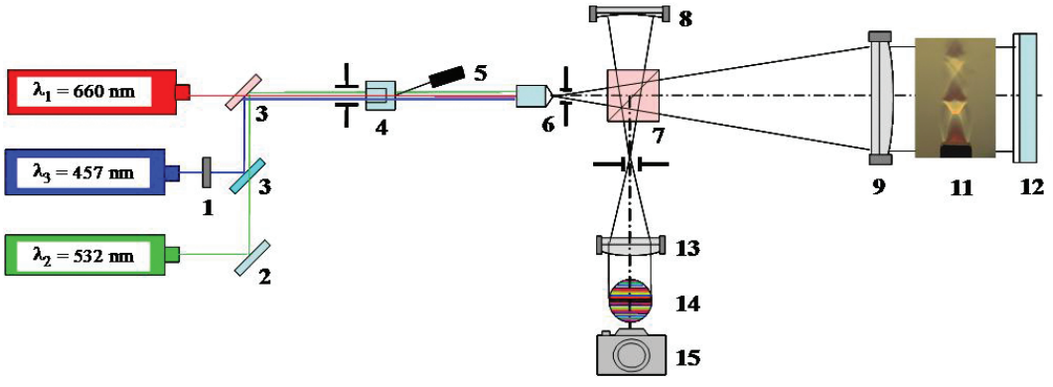

Figure 3. Michelson digital holographic interferometer.

Michelson digital holographic interferometer has been implemented around the ONERA wind tunnel and two optical tables isolate the optical set-up from external vibrations. **Figure 4** shows the generation of micro-fringes used as spatial carrier frequencies.

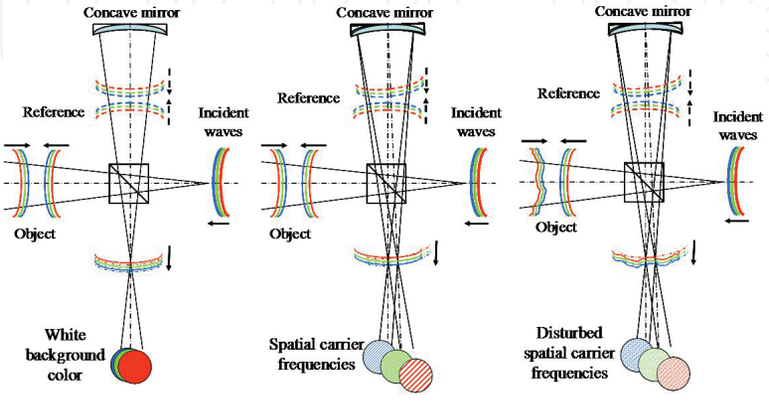

Figure 4. Micro-fringes formation by the transparent object.

http://dx.doi.org/10.5772/66111

When the focal points of the reference and object waves are superimposed in the diaphragm which is placed in front of the lens (13), see **Figure 3**, a uniform background colour is observed on the screen for each colour. The combination of three background colour (R, G and B) produces a white colour on 3CCD camera. If the focusing point of the three reference waves is moved in the plane of the diaphragm, straight interference fringes are introduced into the field of visualization. This is achieved very simply by rotating the concave mirror (8). Without flow, these micro-fringes are recorded on the 3CCD to calculate the three reference phase maps. Then, the wind tunnel is running and the three object waves are distorted by the aerodynamic phenomenon. Micro-fringe interferences are again recorded to enable calculation of the phase maps related to the object. For maps of phase difference, the reference phase is subtracted from the phase object. This optical technique was tested for analysing the supersonic flow of a small vertical jet, 5.56 mm in inner diameter at different pressures of injection. The location of the vertical jet in the middle of the test section is shown in **Figure 3**. The exposure time (10 ms) is given by the acousto-optical cell noted (4) in **Figure 3**. The fringe space introduced in the field is much narrowed, about four or five pixels between two successive fringes, in order to generate three high spatial carrier frequencies. With this configuration, the sensitivity is increased. Each interferogram is processed with 2D fast Fourier transform and **Figure 5** shows the spectra computed for the reference and measurement for each colour plane. One can see that the generated spatial frequencies are respectively equal to 40.5, 30.9 and 28.4 lines per millimetre for the blue, green and red lines. Then, a filtering window is selected to cover the useful signal of the +1 order localized in the spectrum and an inverse 2D FFT is applied to reconstruct the amplitude and the phase of the signal.

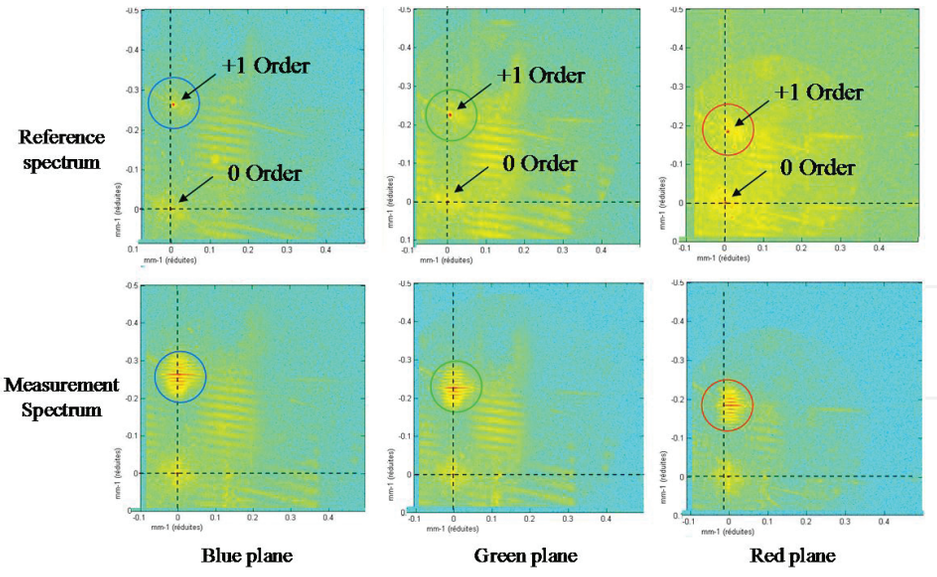

Figure 5. 2D spectra computed from the reference and the measurement interferograms.

First, the phase maps are calculated from the three reference and three measurement spectra so that the modulo 2π phase difference maps shown in **Figure 6**. One can see that the structures of shocks and decompression appear in the jet. As the difference phase maps are computed

modulo 2π, a phase unwrapping has to be conducted and the results given the unwrapped phase maps are also presented in **Figure 6**. At a pressure of 3 bar, we can note a phase variation of 12 rad.

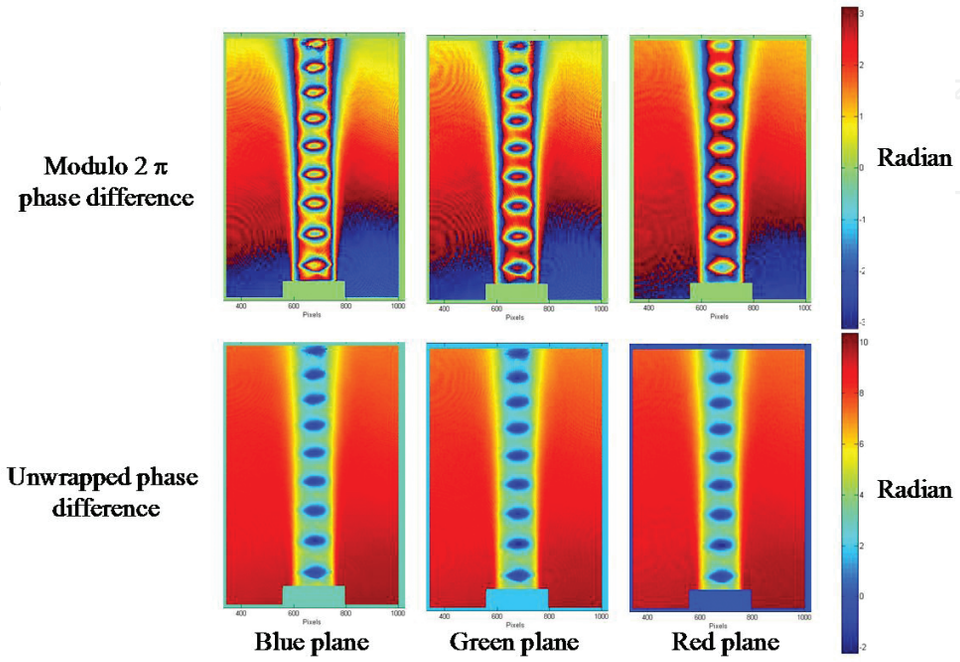

Figure 6. Maps of RGB phase difference (modulo 2π and unwrapped), $P = 3$ bar.

Finally, the maps of light intensity and optical thickness difference are calculated from the phase difference maps. They are presented in **Figure 7** for pressures ranging from 2 to 5 bar.

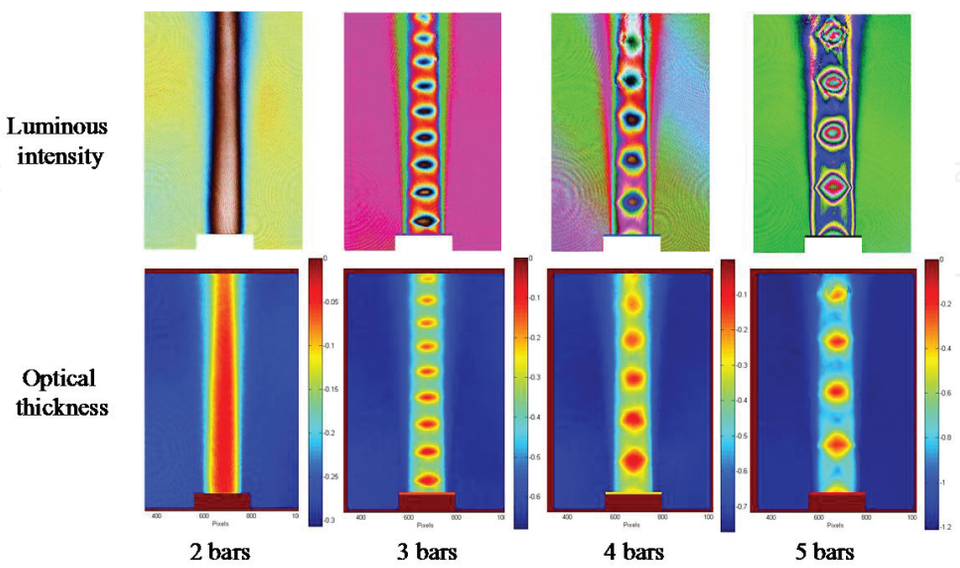

Figure 7. Evolution of the luminous intensity and the optical thickness with the pressure.

http://dx.doi.org/10.5772/66111

Concerning the maps of the luminous intensity, they are corresponding to figures which will be obtained if a technique of image holographic interferometry using panchromatic plates has been used. Knowing the wavelength and the phase, the maps of optical thickness can be deduced. They are also presented in **Figure 7** from 2 to 5 bar. At 2 bar and in the middle of shock structures, the optical thickness varies up to 0.2 μm and at 5 bar, it varies up to 1μm.

3.2. Three-wavelength holographic interferometry using Wollaston prisms

This part proposes an optical set-up based on digital holographic interferometry using two widely shifting Wollaston prisms and a single crossing of the phenomenon. Each Wollaston prism is located at the focal point of 'Z' astigmatic optical set-up. The second Wollaston is located in front of the camera and between the two sagittal and transverse focal lines so that a rotation around the optical axis generates interference micro-fringes which are used as spatial carrier frequency.

3.2.1. Definition of Wollaston prism characteristics

Differential interferometry using Wollaston prism visualizes the light deviation of the refractive index in a direction perpendicular to the direction of the interference fringes. Indeed, in the case of quartz prism having a very weak pasting angle, the gradient of the refractive index is measured because the birefringence angle is very weak and the distance between the two interfering beams is of the order of a few tenths of a millimetre or a few millimetres in the test section. Data integration is necessary to obtain the absolute refractive index. To avoid this integration, it was decided to manufacture two Wollaston prisms having a very high birefringence angle so that the distance between the two interfering beams is greater than the dimension of the measuring field (jet size). The interference measurement will be made between a beam which does not pass through the phenomenon (reference beam) and one which crosses the phenomenon under analysis. If $(n_e - n_o)$ is the crystal birefringence and α, the pasting angle of prisms, the birefringence angle ϵ can be expressed using the following equation:

$$\varepsilon = \varepsilon(\lambda) = 2(n_e - n_o)\tan(\alpha) \tag{1}$$

If a very high birefringence angle is sought, the pasting angle and the crystal birefringence have to be as high as possible. To remember, the Δn birefringence values for quartz and calcite are, respectively, equal to +0.009 and −0.172. It can be seen that calcite birefringence is basically twenty times greater than quartz birefringence.

If R is the radius curvature of the spherical mirror used in the optical set-up, the shift dx between the two interfering beams can be written as:

$$dx = \varepsilon R = 2R(n_e - n_o)\tan(\alpha) \tag{2}$$

Thus, for a spherical mirror of 400 mm in diameter and 4 m in the radius of curvature, *dx* has to be near to 200 mm. By choosing calcite crystal, the pasting angle can be found from the following relationship:

$$\alpha = \arctan\left(\frac{dx}{2R\Delta n}\right) = \arctan\left(\frac{0.2}{8x0.172}\right) = 8.27° \tag{3}$$

Calcite Wollaston prisms with 8° pasting angle have been manufactured.

3.2.2. Optical set-up with single crossing of the test section

Figure 8 shows the principle of Z optical set-up using Wollaston prisms. Here also, three different DPSS lasers (red, green and blue) constitute the luminous light source and the optical set-up uses two spherical mirrors, 250 mm in diameter and 2.5 m in radius of curvature.

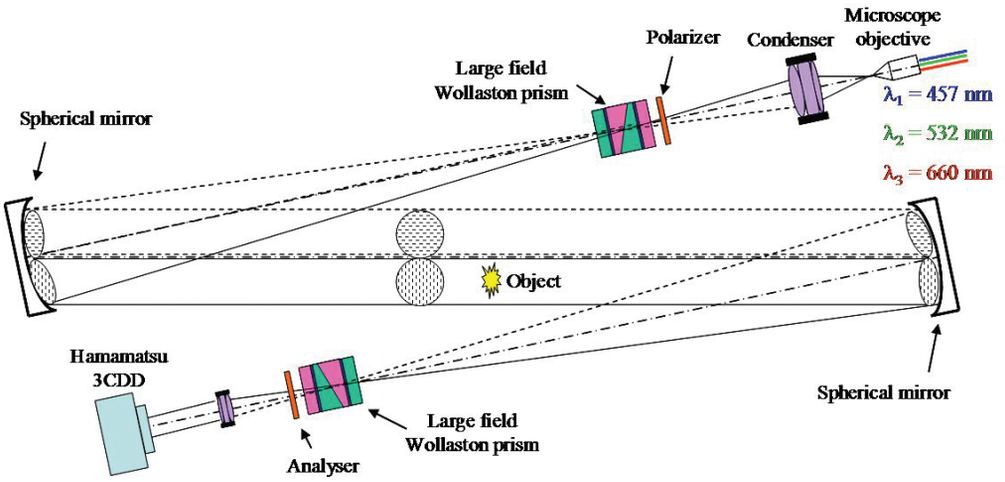

Figure 8. Digital holographic interferometer using very large Wollaston prisms in 'Z' set-up.

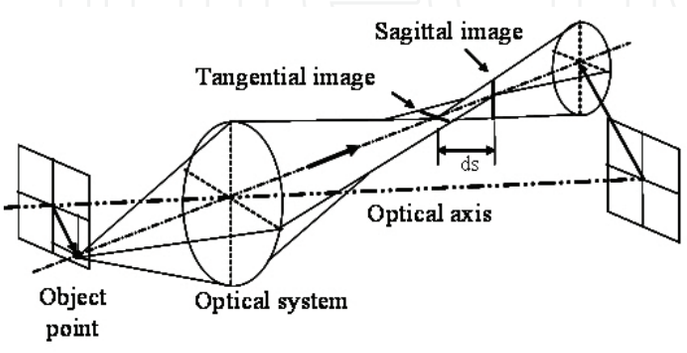

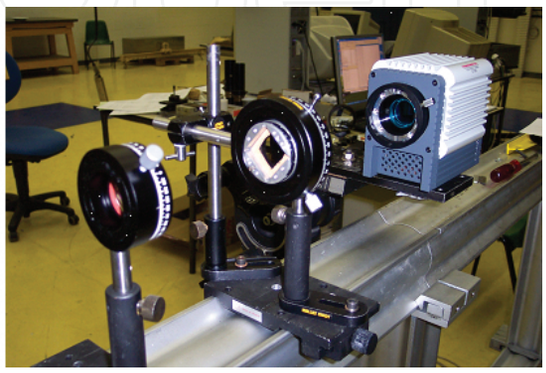

Figure 9. Astigmatism represented by sectional views and Wollaston prism in the front of the camera.

http://dx.doi.org/10.5772/66111

As all optical pieces are not exactly on the optical axis of spherical mirrors, we can observe astigmatism in the optical arrangement. The first prism located at the focal length of the first spherical mirror produces two optical rays which are returned by parallel light beams onto the second spherical mirror. This one refocuses the light beam into the second Wollaston prism which is mounted 'tumble' with the first one. An analyser located behind the second prism allows visualizing the interference fringes in colour. The image of the object under analysis is formed by a field lens placed in front of the 3CCD sensor. Here, the advantage of astigmatic set-up is used because the focusing point in the front of the camera is not unique. **Figure 9** shows this particularity: the optical beams are focused on the two focal images successively separated by a few millimetres. The first one gives the tangential image encountered when the beam focuses in the horizontal plane, and the second one, called the sagittal image, is obtained when the beam focuses in the vertical plane.

Figure 10 shows, on the reception side, the different figures of interference observed when the second Wollaston prism is moved along the optical axis from the tangential image (TI) towards the sagittal image (SI). The interference fringes which were horizontal and much narrowed, spread. When the interference fringes spread again, we can observe a rotation of 90° by them to give a quasi-uniform vertical background colour, at half distance between the tangential and sagittal images. Then, they continue to rotate by 90° up to the sagittal image and they narrow to become horizontal. Interference fringes stay horizontal above the sagittal image and narrow more and more. Knowing this property, we can adjust the spatial carrier frequency by the axial displacement of the prism for its amplitude and by rotating the prism for its orientation. In our tests, the Wollaston prism is located at half distance between the tangential and sagittal images, so that the interference fringes are generated in the same direction as the direction of the two interfering beams (vertical shift and vertical fringes). Gontier et al. [13] has widely described this feature. If the number of fringes in the visualized field has to be increased, the Wollaston prism has to be turned on itself in the plane perpendicular to the optical axis. **Figure 10** shows two positions of rotation of the Wollaston prism (20 and 45°) with a maximum number of fringes obtained for the rotation of 45°.

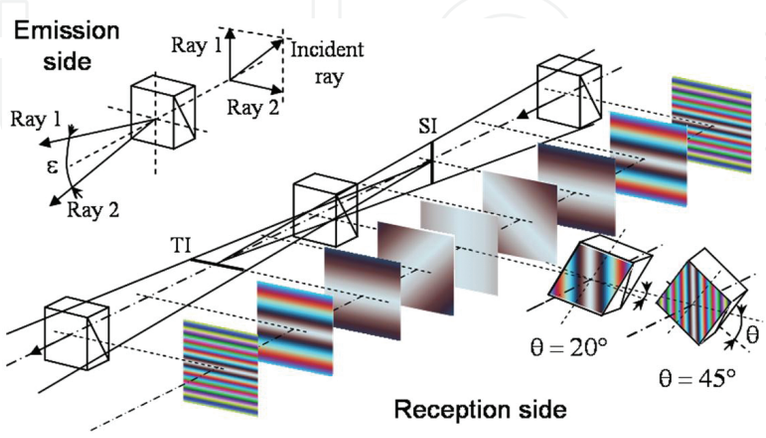

Figure 10. Evolution of interference fringes when the second Wollaston is moved from the sagittal image to the tangential image.

3.2.3. Results obtained

First, **Figure 11** shows the interferograms for the reference and the measurement with an enlarged view near the injection. For a pressure of 4 bar, for instance, one can see the horizontal interference fringes disturbed by the flow. The interferograms of **Figure 10** also show that the field is reduced on the right and left sides: this is the result of the rotation of the Wollaston prism at return which has a limited size (15 mm^2). The polarization fields which were completely separated on the way interfere with each other as the prism placed in front of the camera is rotated. It is also noteworthy that the polarizer is rotated exactly to the same amount as the Wollaston prism. The tightening of the fringes is maximal when the prism is rotated by 45°.

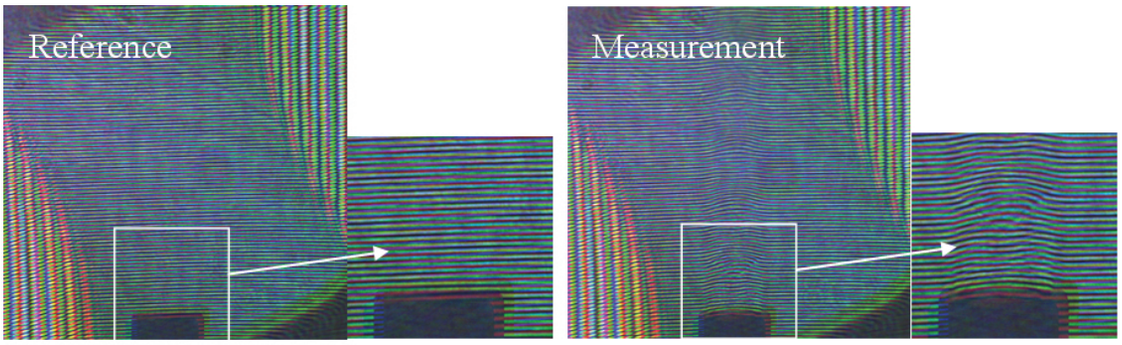

Figure 11. Interference micro-fringes recorded for the reference and the measurement, P = 4 bar.

Then, 2D fast Fourier transform is applied to filter the zero and -1 orders on the three channels for the reference and the measurement interferograms. In **Figure 12**, one sees that the different window filtering size can be taken on the three channels and that the reduced frequencies are equal to 0.12, 0.10 and 0.9 mm^{-1} for the blue, green and red channels that correspond to resolution of 18.6 lines/mm, 15.5 lines/mm and 13.9 lines/mm. The spatial resolution used is lower than that used in the technique of Michelson interferometry.

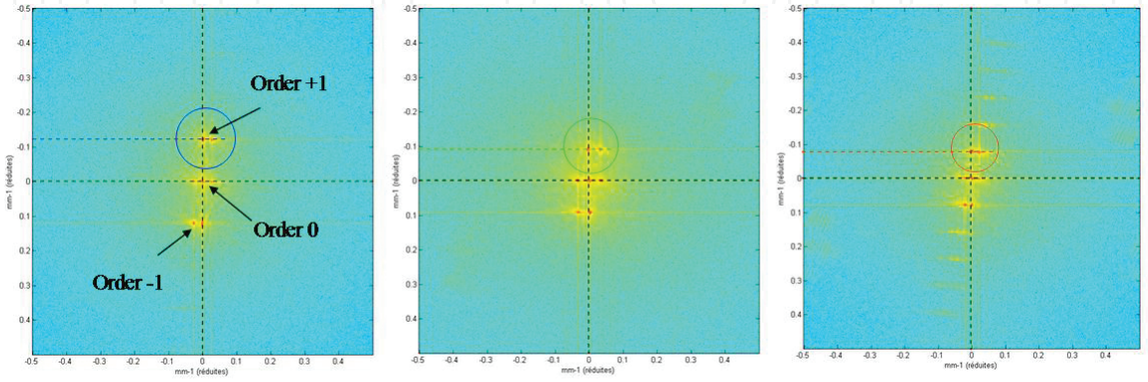

Figure 12. 2D spectra computed on the three channels for the reference interferogram, P = 4 bar.

http://dx.doi.org/10.5772/66111

Figure 13 shows the spectrum of the measurement for P = 3 bar, the modulo 2π phase map, the superimposition of the three red, green and blue luminous intensities deduced from the phase difference maps and also the optical thickness map computed from the phase difference map. These maps are concerning the red channel. Moreover, a deconvolution of the optical thickness maps based on the assumption that the jet is axisymmetric has been applied. Thus, it is possible to obtain the radial distribution of the refractive index and the density in the jet according to the relation proposed by Gladstone-Dale. This method is widely described by Rodriguez et al. [14]. In the treatment process, the optical thickness of maps calculated for each jet pressure is split into two parts, on either side of the axis of symmetry of the jet. If the results found by both sides of the jet are identical to the symmetry axis, the assumption of the axial jet symmetry is verified and the results can be considered correct. In **Figure 12**, the radial gas density is presented at 3 bar, and the density values found on the axis are very close, the analysis being done on the right or on the left.

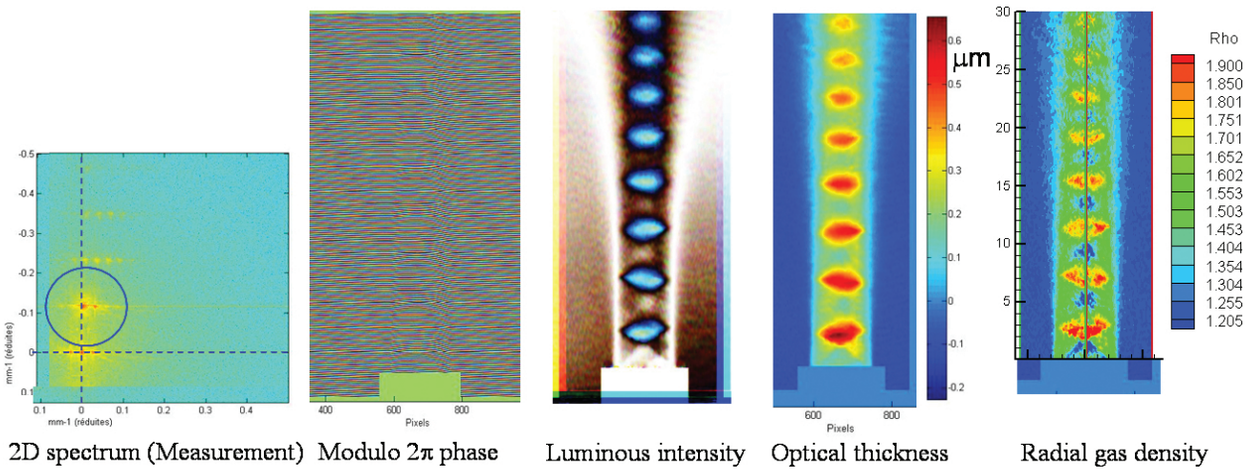

Figure 13. Analysis of the case for red channel P = 3 bar (from spectrum to gas density).

3.3. Digital holography without reference wave

Digital holography without reference wave allows quantitative phase imaging by using a high-resolution holographic grating for generating a four-wave shearing interferogram. The high-resolution holographic grating is designed in a 'kite' configuration so as to avoid parasitic mixing of diffraction orders. The selection of six diffraction orders in the Fourier spectrum of the interferogram allows reconstructing phase gradients along specific directions. The spectral analysis yields the useful parameters of the reconstruction process. The derivative axes are exactly determined whatever the experimental configurations of the holographic grating. The integration of the derivative yields the phase and the optical thickness [12].

3.3.1. Base of digital holography without reference

Figure 14 shows the principle of the hologram recording of pure phase modulation where an incident plane crosses the phenomenon under analysis. This wave, disturbed by the phenom-

enon, is simultaneously diffracted in several directions by a diffraction grating operating in reflection. The different images diffracted by the grating interfere with each other at a δz distance of the diffraction plane.

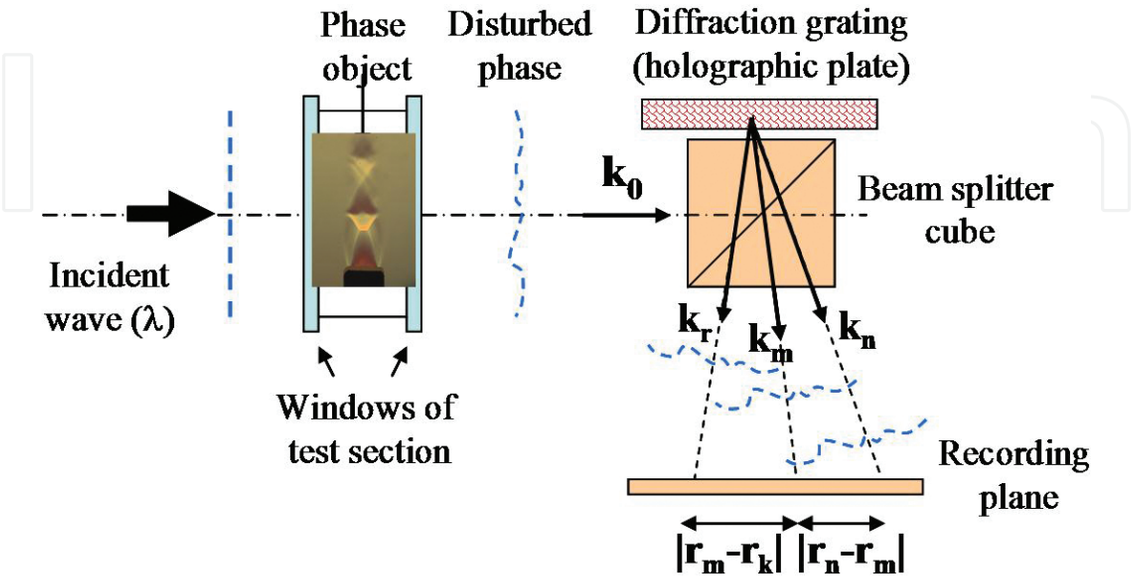

Figure 14. Principle of self-referenced digital holography by reflection.

The sensor therefore records a digital hologram produced by the coherent superimposition of all the diffraction orders. Let $A(r')$ the complex object wave front in the object plane, and $O(r) = A_o(\mathrm{r})\exp(i\varphi_o(r)(i = \sqrt{-1})$ the wave front diffracted from the object plane to the recording plane (**r** is the vector of the Cartesian coordinates $\{x, y\}$ in the plane perpendicular to the z direction). The reflection of the incident wave on the holographic grating produces a set of replicated waves, whose propagation direction is given by their wave vector $k_n = 2\pi/\lambda e_n$ (e_n is the unit vector of the propagation direction). The amplitude of the diffracted wave front at the recording plane is expressed as:

$$O(r, k_n) = A_o(r - r_n)\exp(ik_n r + i\varphi_o(r - r_n)) \tag{4}$$

In Eq. (4), r_n is the spatial shift produced by propagation along distance δz from the holographic plane and in the direction of unit vector e_n. Due to the holographic grating, $P = 4$ wave fronts (n varying from 1 to $P = 4$) are diffracted in different directions. The interferogram recorded in the sensor plane is written as:

$$H(r) = \sum_{n=1}^{n=P} A_O^2(r - r_n) + 2\Re\left\{\sum_{n=1}^{P-1}\sum_{m=n+1}^{P} O(r, k_n)O^*(r, k_m)\right\} \tag{5}$$

http://dx.doi.org/10.5772/66111

In Eq. (5), the first term is related to the zero order, and the last one is related to coherent cross-mixing between the P diffracted orders. The last term includes the useful data related to the phase at the object plane. Noting $\Delta\varphi_{nm}$ the phase of cross-mixing $O(r,k_n)O^*(r,k_m)$, we get:

$$\Delta\varphi_{nm}(r) = (k_n - k_m)r + \varphi_0 - r - r_n) - \varphi_0(r - r_m) \tag{6}$$

Eq. (6) can be simplified by considering spatial derivatives of the object phase according to:

$$\Delta\varphi_{nm}(r) \cong (k_n - k_m)r + |s_{nm}|\frac{\partial\varphi_0(r)}{\partial re_{nm}} \tag{7}$$

In Eq. (7), e_{nm} is the unit vector of vector $s_{nm} = r_n - r_m$ and $\left(k_n - k_m\right)r$ is the spatial carrier phase modulation. In the Fourier plane of the interferogram, the diffraction orders are separated from the zero-order diffraction and localized by the spatial frequency vector $(k_n - k_m)/2\pi$. Since they are localized at different spatial frequencies in the Fourier domain, they can be filtered in the same way as for off-axis interferometry. Then, the spatial carrier frequency is removed. Note that spatial derivatives of the object phase are provided along an axis given by the scalar product re_{nm}. The scaling of each spatial derivative is related to $\left|s_{nm}\right|$. Thus, it appears that the method provides spatial derivatives with different sensitivities, which depend on the geometric configuration of the diffraction orders. After extracting each useful order, the term $\left|s_{nm}\right|\partial\varphi_0/\partial re_{nm}$ is extracted from the argument of the inverse Fourier transform of the filtered interferogram spectrum. We note $\partial\varphi_0/\partial re_{nm} = \partial\varphi_0/\partial x_q$, $\left|s_{nm}\right| = \alpha_q$ and $D_q = (1/\alpha_q)\left|s_{nm}\right|\partial\varphi_0/\partial re_{nm}$, with q varying from 1 to Q, Q being the number of really independent axis re_{nm} amongst the set of the useful orders included in the spectrum. So, the spatial variable x_q is simply the direction of the axis along which the derivative operator operates. In the spatial frequency domain, this axis has a corresponding axis which will be referred as u_q. Note that, from a computational point of view, x_q and u_q are 2D vectors. In case that D_q exceeds 2π, phase jumps occur and phase unwrapping is required. The scaling coefficient α_q depends on the distance δz and on the couple of involved wave vectors (k_n, k_m). Then, the spatial integration of terms D_q has to be carried out to get the quantity ψ. The wave-front reconstruction problem has already been discussed by many authors and the methods are based on least-square estimations or modal estimations. Note that in these works the wave front differences are defined at each point according to the sensor sampling geometry. In the modal approach, the wave front and its differences are expanded in a set of functions and the optimal expansion coefficients are determined (for example, using Zernike and Legendre polynomials). Here, the numerical method is based on the weighted least square criterion and according to Refs. [15, 16], quantity ψ can be recovered.

3.3.2. Design of diffraction grating

First, a holographic grating is recorded with the optical set-up shown in **Figure 15**. The holographic plates are single-layer silver-halide holographic plates from Gentet (http://www.ultimate-holography.com/). The spatial resolution reaches 7000 lines per mm and the holographic plate has been preferred to the photopolymer which has lower spatial resolution (1000–2000 lines per mm).

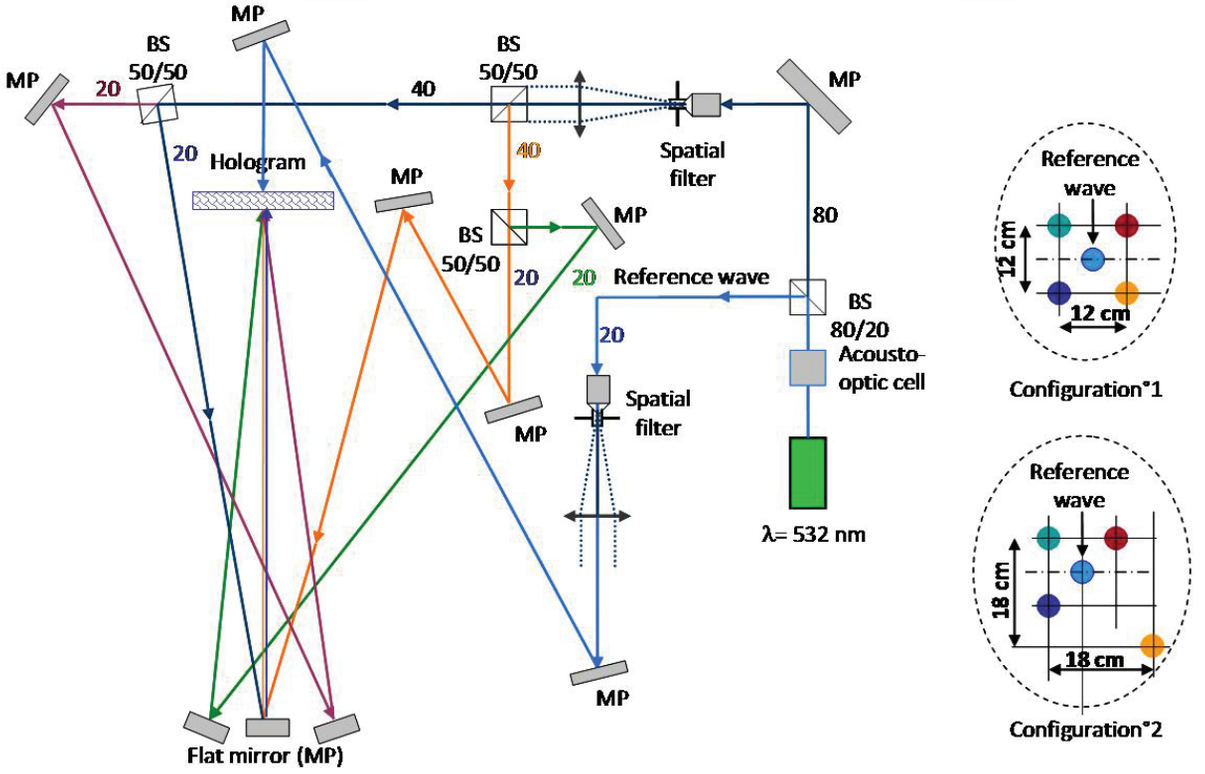

Figure 15. Optical set-up defined for recording of reflection holographic grating.

A first beam splitter cube (80/20) forms a reference beam (blue beam) with 20% of the incident light and 80% of the light is used to form the four-object beams. Plane waves are obtained with two lenses and two spatial filters. Object waves are generated by three-beam splitter cubes (50/50) so that the luminous intensities of each beam (reference and object) are all equal to 20% of the initial laser power. After several reflections on flat mirrors (MP), four small mirrors located around a square (configuration no. 1) and around a kite (configuration no. 2) returns each object beams towards the holographic plate. As the reference wave and the four object waves are incoming on each side of the hologram, the hologram is recorded by reflection and the angle θ formed by the reference and the object waves are equal to 27 mrad for configuration no. 1. After four sequential exposures, one for each object wave, the holographic plate is developed and bleached. Then, the grating is inserted in the optical set-up which is used for analysing the small supersonic jet from a nozzle. **Figure 16** shows the optical set-up with a single crossing of the phenomenon at the distance δz between the sensor and the image of the high-resolution holographic grating (HRHG).

http://dx.doi.org/10.5772/66111

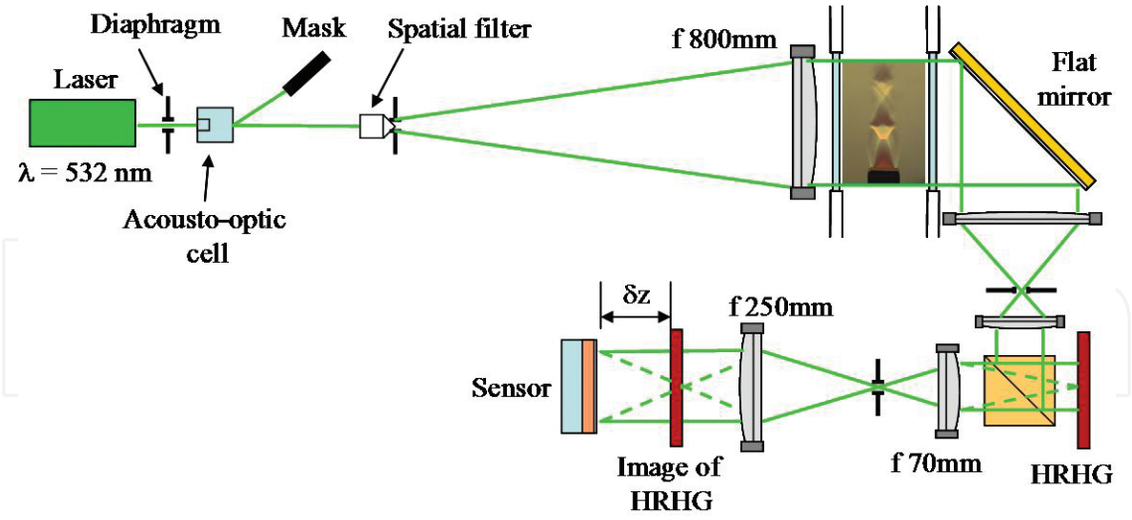

Figure 16. Digital holographic interferometer without reference.

An interferogram without flow and another with flow are directly recorded on the sensor (2000 × 1500 pixels, 365 mm^2), then analysed in delayed time by 2D fast Fourier transform in order to localize the different interference orders. For configuration no. 1, **Figure 17** shows the location of four mirrors used at the recording (square). Order 1 results of interaction of the beams incoming from M1 and M2 mirrors and the order 1′ between M3 and M4. Similarly, order 2 is generated by the interference between the waves incoming from M1 and M3 mirrors and order 2′ those issuing from M2 and M4. Order 3 is only produced by the interference between M1 and M4 and order 4 between M2 and M3. For configuration no. 1, order 1 or 2 has been enlarged in order to show that order 1 and 1′ or 2 and 2′ are not quite superimposed.

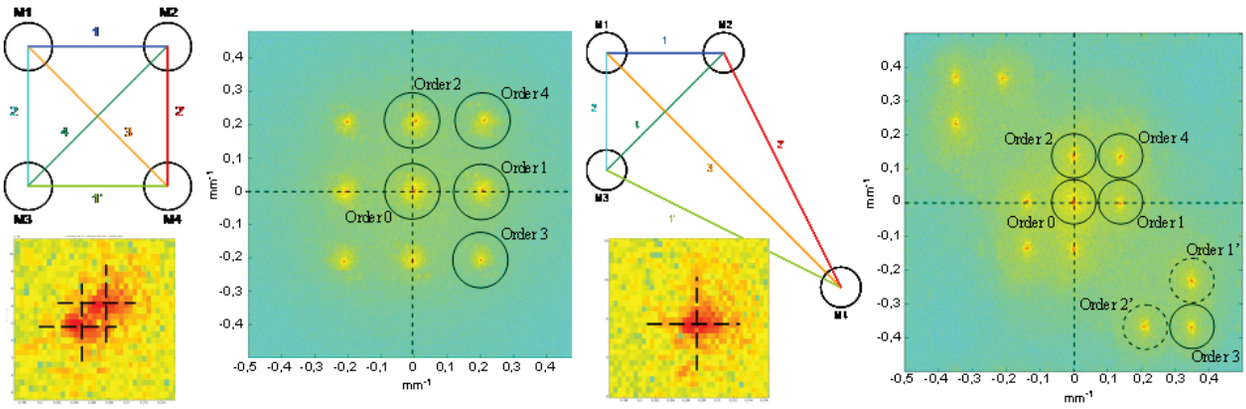

Figure 17. Position of four mirrors (square and kite) at the recording, localization of different diffraction orders in 2D FFT plane and zoom of +1 order.

In fact, one obtains two spectral signatures slightly shifted. It is not possible to separate them by filtering and to reconstruct the phase derivative map induced by only order 1. For this reason, the four mirrors have been set at the four tops of a kite configuration (no. 2). The problem encountered with configuration no. 1 does not exist and 2D FFT shows that it is very

easy to localize all the different diffraction orders (on right in **Figure 17**). There is no spectral overlap and all orders useful for the reconstruction are well separated. Each order of interference is then selected successively and separately with a circular mask (0.05 mm^{-1} radius). Then, the phase gradient of reference image is calculated for each order of interference (**Figure 18**). Subtracting the reference image to the measurement image gives a modulo 2π map of phase gradient difference caused by the flow. Then, difference phase maps have to be unwrapped and results are presented in **Figure 18** for the six diffracted orders and for a value of the generating pressure equal to 5 bar. Finally, knowing the phase gradient difference in the six directions, a reconstruction of the absolute phase map is possible. For this processing of integration calculation, one can use one of integration methods proposed in the literature, for instance that proposed by Frankot and Chellappa [15]. The modulus of complex amplitude and the optical phase of the diffracted field by the object can be combined for obtaining the complex wave diffracted in the sensor plane.

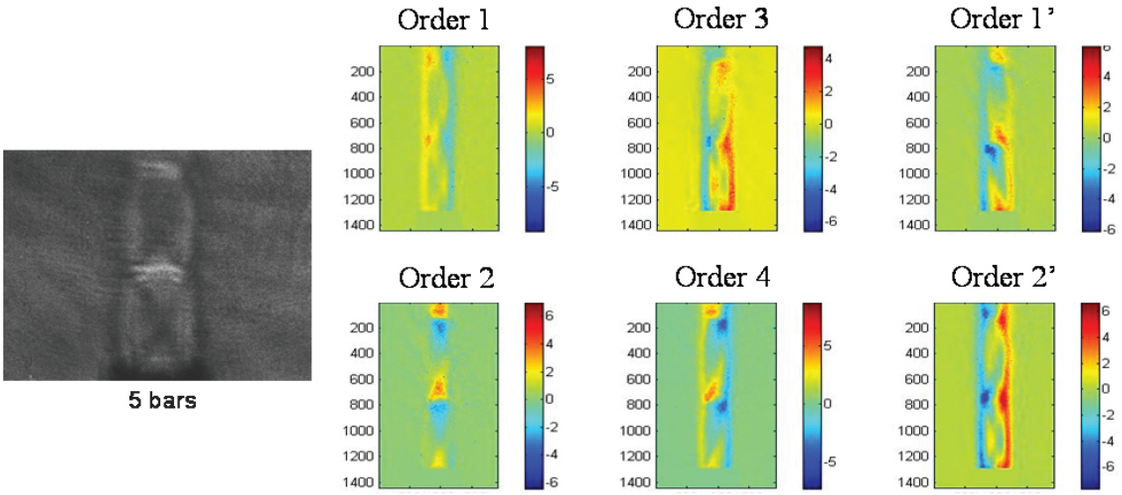

Figure 18. Recorded interferogram and gradient phase maps obtained for the six interference orders.

3.4. Comparisons with digital holographic interferometry using a reference wave

Figure 19 shows results obtained with digital holographic interferometry without reference and two other results obtained with digital holographic interferometry using a reference wave. The comparison is made by taking into account the difference of optical thickness.

The scale level is basically the same for the three results (from 0 up to 1.2 μm), and **Figure 19** shows at 5 bar that they are in good agreement because spatial locations of the structures of compression and expansion waves are similarly positioned in the three measurements. From a point of view of easiness and accuracy of results, the optical set-up without reference is complicated to implement and must achieve a kite-type reference hologram. It is also difficult to obtain a hologram with high diffraction efficiency. In addition, the data obtained must be integrated, which cause a certain imprecision in the measurement. For the optical set-up using Wollaston prisms, it is very bulky and costly because the Wollaston prisms of 'large field' type

http://dx.doi.org/10.5772/66111

are expensive and difficult to manufacture. On the other hand, the measured values are absolute values as those obtained with Michelson interferometer that seems the least restrictive optical arrangement of the three set-ups tested.

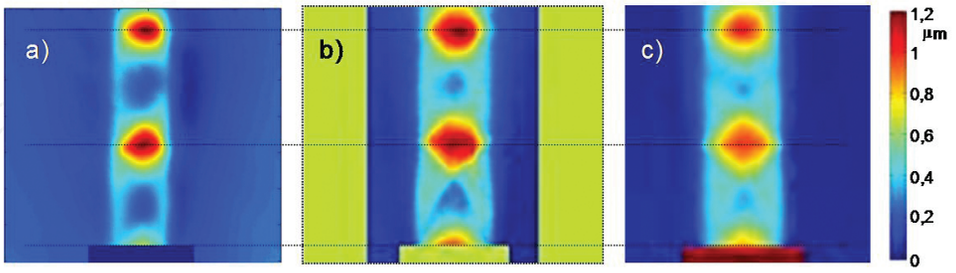

Figure 19. Comparison of experimental results obtained for three different interferometric techniques for a pressure at P=5 bar. (a) Without reference set-up, (b) Michelson set-up, (c) Wollaston set-up.

4. Digital holography for analysing unsteady wake flows

The unsteady wake flows generated in wind tunnel present a large scale of variations in refractive index from subsonic to supersonic domain. The feasibility of three-wavelength digital holographic interferometry has been shown on two-dimensional unsteady flows and the time evolution of the gas density field has been determined on the subsonic near wake flow downstream a circular cylinder [8]. But, when the flow regime reaches the transonic or supersonic domain, problems appear because refractive index gradients become very strong and a shadow effect superimposes to the micro-fringes of interferences. Moreover, the displacement of vortices is very high compared to the exposure time (300 ns given by the acousto-optical cell, **Figure 3**) what leads to blurred zones in interferograms and limits the interferograms analysis (**Figure 20**).

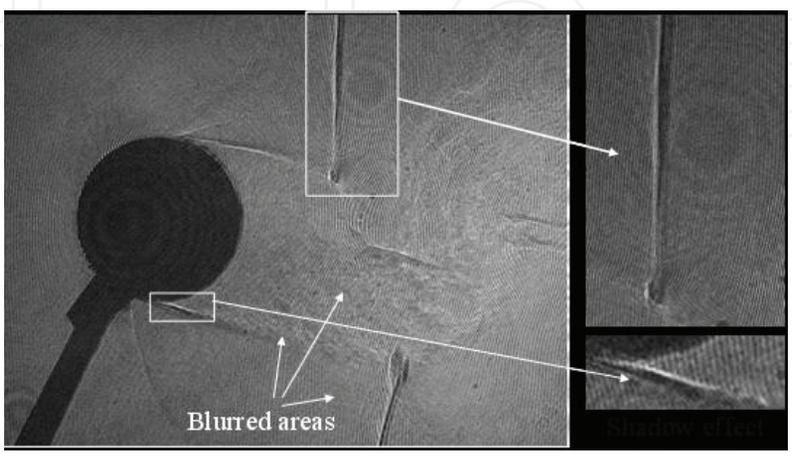

Figure 20. Highlighting of blurred areas and shadow effect—Mach 0.73.

4.1. Michelson holographic interferometry

At first, an ORCA Flash 2.8 camera from Hamamatsu with a matrix of 1920 × 1440 pixels, 3.65 μm^2, has been bought to increase the spatial resolution and, for the temporal resolution, the continuous laser light source of the interferometer has been replaced by a Quanta-Ray pulsed laser, Model Lab 170-10 Hz from Spectra-Physics. This laser is injected through a 1064 nm laser diode and outputs a wavelength at 1064 nm having 3 m in coherence length (TEM00 mode). Here, the first harmonic is used (532 nm) and delivers about 400 mJ in 8 ns. The beam diameter is about 8–9 mm. **Figure 21** shows how the laser was installed in Michelson interferometer presented in **Figure 3**. The output beam is equipped with two sets 'λ/2-polarizing beam splitter cube' to significantly reduce the laser energy sent to the camera. It is seen in **Figure 21** that the beam splitter cube forms the reference wave which is reflected by the concave mirror on the camera and the measurement wave which passes through the test section. The second achromatic lens, 70 mm in focal length of 70 mm yields the magnification of the image on the CCD.

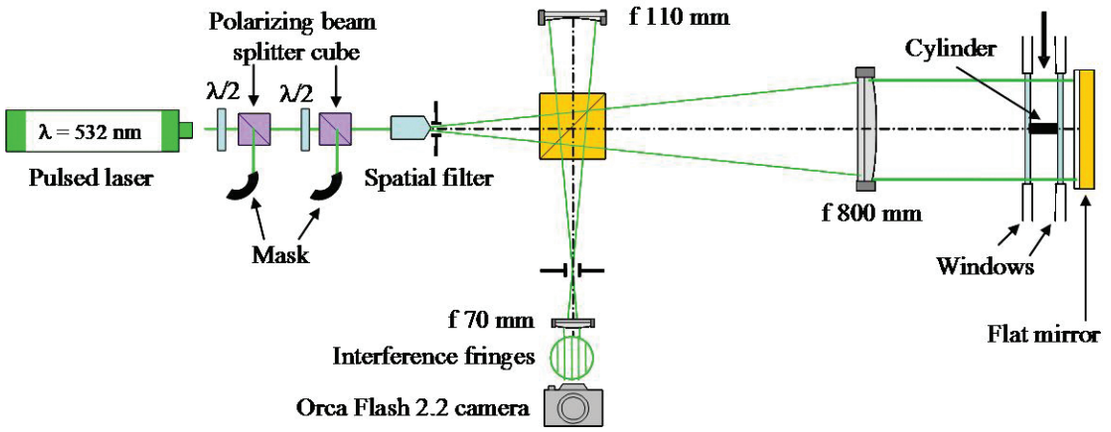

Figure 21. Digital Michelson holographic interferometer using a pulsed laser.

If L_1 is the distance between the beam splitter cube and the concave mirror, and L_2 the distance between the same beam splitter cube and the flat mirror located behind the test section, the laser coherence length must be greater than twice the difference ($L_2 - L_1$) for the interference fringes may be formed on the CCD. This difference is here of the order of 2.5 m.

Figure 22 shows an interferogram of unsteady wake flow around a circular cylinder at Mach 0.73 with Michelson interferometer, the 2D FFT spectrum with the +1 order used to reconstruct the map of the modulo 2π phase difference. The interferogram exhibits a good quality indicating that vortex structures and small shock waves are well frozen. But, in the modulo 2π phase difference map shown on the right of **Figure 22**, phase jumps are still present. They are surrounded by black ellipses on the figure and they will cause phase shifts during the unwrapping of the modulo 2π phase map. To decrease the sensitivity of the measurement by a factor of 2, the optical bench has been modified to create a Mach-Zehnder type bench.

http://dx.doi.org/10.5772/66111

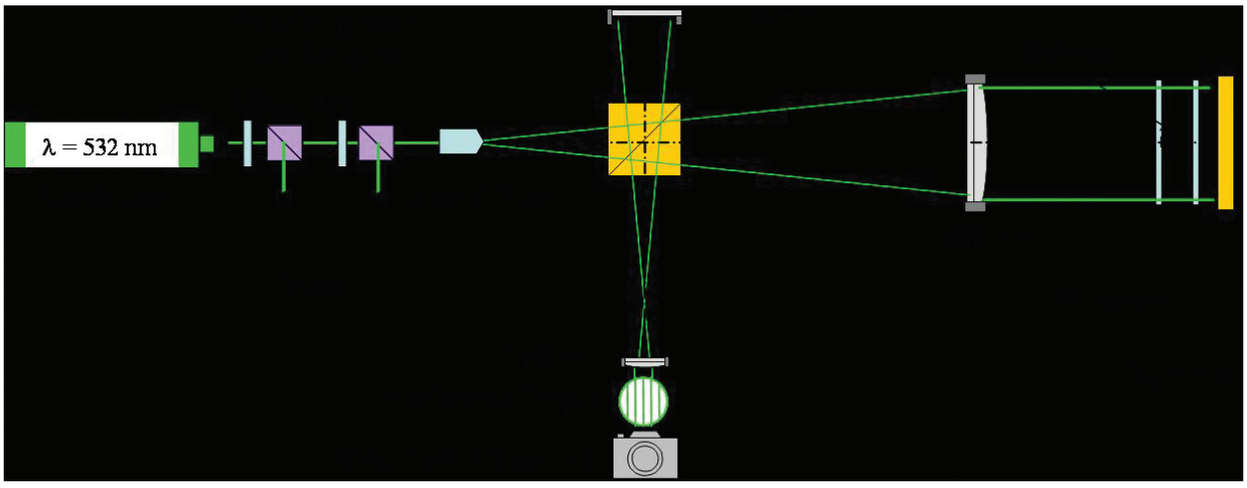

Figure 22. Interferogram analysis at Mach 0.73—residual phase shifts.

4.2. Mach-Zehnder holographic interferometry

In Mach-Zehnder interferometer, shown in **Figure 23**, the measuring beam crosses only once the test section and the reference beam passes outside the test section so that the sensitivity is decreased by a factor 2.

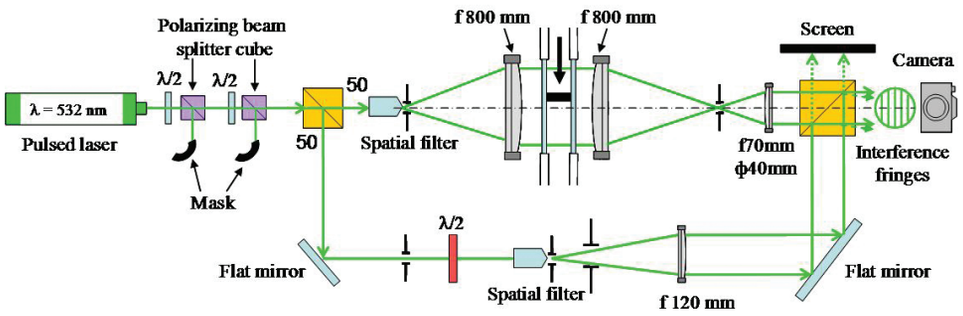

Figure 23. Digital Mach-Zehnder holographic interferometer using a pulsed laser.

In this optical set-up, the reference beam is reflected successively by several little flat mirrors. That produces a polarization rotation of the reference wave which must be corrected by inserting a $\lambda/2$ plate in front of the spatial filter of the reference wave. The contrast of the interference fringes can thus be optimized on the interferogram. The cylinder is equipped with an unsteady pressure transducer at a 90° azimuth to the flow axis in order to correlate the laser pulse with the signal of unsteady pressure. In this manner, one period of the phenomenon can be sampled by 20° step with several different tests. First, in the enlarged part of reference and measurement interferograms of **Figure 24**, one can see the straight interference micro-fringes distorted by the shear layer incoming from the upper of the cylinder. 2D FFT spectra show that the spatial carrier frequency (vertical fringes) is localized on horizontal axis (order +1 of hologram). After applying a spatial filter around the first order and subtracting the reference

to the measurement phase map, one obtains the modulo 2π phase difference map where no phase shifts appear.

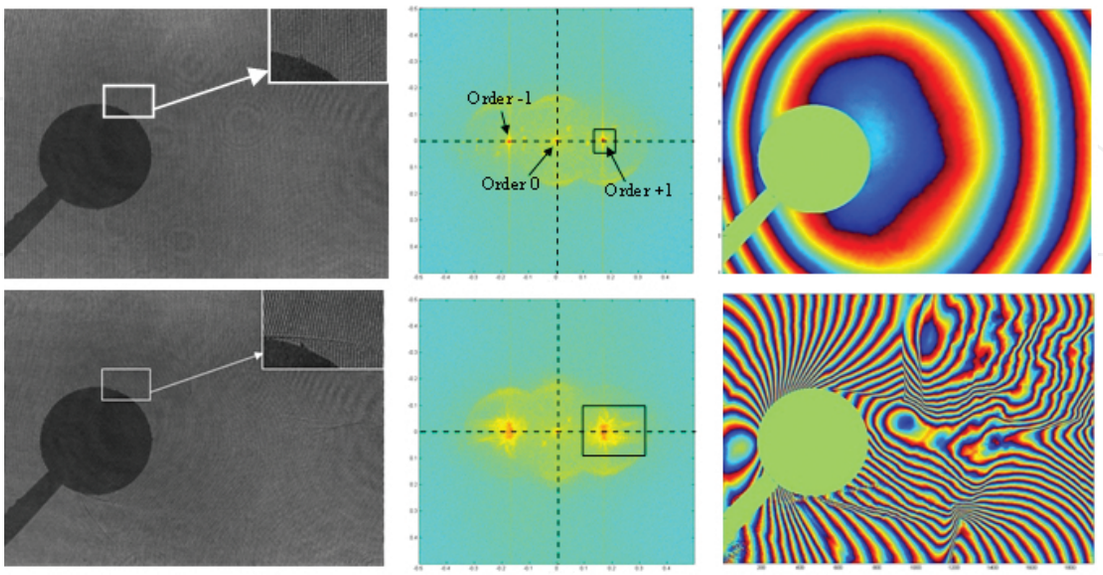

Figure 24. Interferograms analysis at Mach 0.73.

Then, an unwrapping has to be applied to obtain the phase difference map $\Delta\theta$ and the gas density field ρ/ρ_0 presented in **Figure 25** is deduced from the Gladstone-Dale relationship and Eq. (8) is obtained:

$$\frac{\rho}{\rho_0} = 1 - \left(\frac{\rho_s}{\rho_0} \frac{\lambda \Delta\phi}{2\pi e K} \right) \tag{8}$$

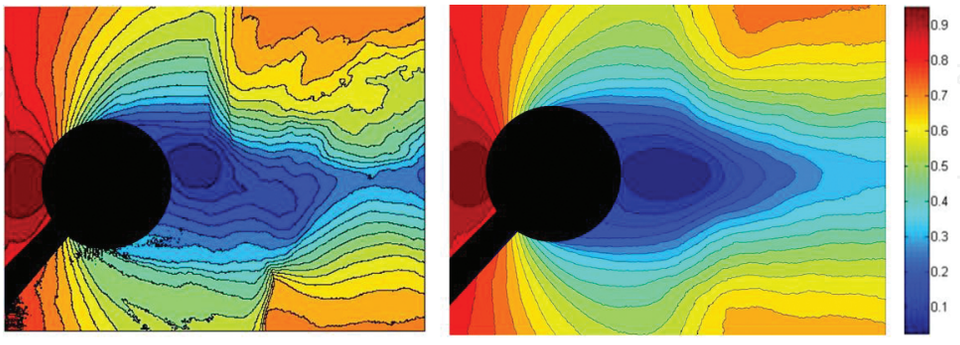

Figure 25. Instantaneous and averaged gas density fields (ρ/ρ_o)—Mach 0.73.

where ρ_s is the standard gas density computed at 1 atm and 0°C, ρ_0 the stagnation gas density, λ the wavelength of the interferometer, e the width of the test section and K the Gladstone-Dale constant: 296×10^{-6}.

http://dx.doi.org/10.5772/66111

The instantaneous interferogram of **Figure 25** shows that shock waves emitted by the vortices of the vortex shading are very well analysed (no phase shift) and the averaged gas density field exhibits a strong decreasing of the gas density just behind the cylinder up to 90% of ρ_0.

For information, the shadow effect can be easily reduced. If the beam of the reference arm is blocked (see **Figure 23**), the Mach-Zehnder interferometer looks like to shadowgraph optical set-up. In these conditions, the sensor can be adjusted along the optical axis to focus and image the middle of the test section on the sensor. As this condition is reached, the shadow effect is minimized.

5. Digital holography for visualizing inside strongly refracting transparent objects

High-density gradients can also exist inside strongly refracting objects and the visualization and the measurement of these phenomena remain an open problem. For example, objects as a glass ball, a light bulb, a glass container, a glass flask, etc. are not opaque but they are strongly refracting light and measuring inside is not straightforward. It follows that observing phenomena, such as refractive index variations, convection currents, or thermal gradients, occurring inside the object requires specific methods. Different experimental methods are usually used to investigate fluids and to visualize/measure dynamic flows [7, 8, 17]. Nevertheless, these approaches are appropriated when the envelope including the flow is relatively smooth and transparent (i.e. not strongly refracting). A suitable experimental method should be able to exhibit the phase changes inside the object without suffering from any image distortion. The experimental approach described here is based on stochastic digital holography to investigate flows inside a strongly refracting envelope [18]. It leads to the measurement of the phase change inside the object, so as to get a quantitative measurement. Experimental results are provided in the case of the visualization of refractive index variations inside a light bulb and a comparison with image transmission and reflection holography is also provided.

5.1. Proposed method

The approach adapted to visualize inside a strongly refracting object is described in **Figure 26**. The sensor includes $N \times M$=1920 × 1440 pixels with pitches $p_x = p_y$ = 3.65 μm. The main feature is that a diffuser is used to illuminate the object to provide a back illumination. The set-up exhibits some similarity compared to a classical transmission microscope, although, no microscope objective is used and the illuminating wave is quite a speckled wave. A negative lens is put in front of the cube to virtually reduce the object imaged by this lens. This leads to a more compact system compared to the case where the lens is not used. For example, for an object size of 10–15 cm, the distance d_0 in **Figure 26** has to be greater than 2 m. The use of the negative lens produces a smaller image of the image, whose position is close to the sensor [19, 20]. Thus, the distance that has to be used in the algorithm is d'_0 (see **Figure 25**). The optimization of the off-axis the set-up has to follow the basic rules about the Shannon conditions [21].

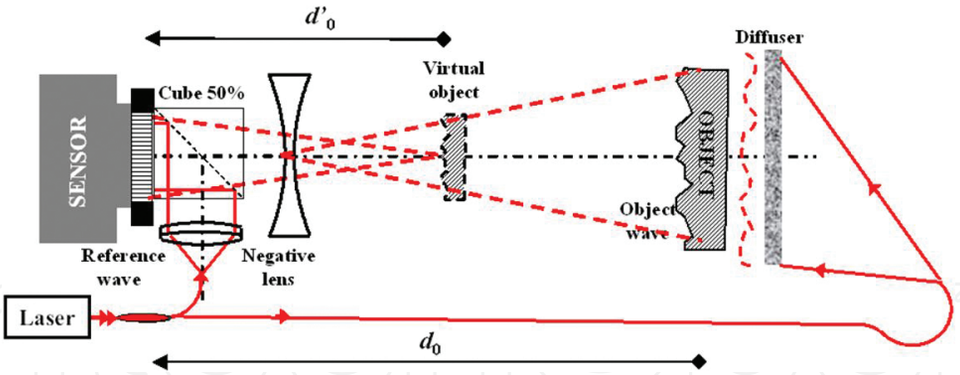

Figure 26. Stochastic digital holographic set-up.

In particular, the focal length of the lens has to be judiciously chosen. Especially, the criterion is the observation angle θ_{max} from the sensor, which has to fulfil this condition:

$$\theta_{max} = \frac{\lambda}{(4-2\alpha)\max(p_x, p_y)} \tag{9}$$

where α is the accepted tolerance in the superposition of the useful +1 order and the 0 order. Here, the diffuser (considered here as a 'stochastic screen') is sized 10 cm × 20 cm and a superposition tolerance of α = 20% is accepted. The evaluation of the focal length and distance leads to d_0 = 800 mm, d'_0 = 100 mm and f'=−150 mm. Holograms can be reconstructed by the adjustable magnification method described in [22] or by the discrete Fresnel transform [19–21]. After reconstruction of the complex amplitude in the virtual object plane, an amplitude image and a phase image can be calculated. The amplitude image is related to the image of the object given by the lens, whereas the phase is useful to investigate refractive index variations, convection currents, or thermal gradients, occurring inside the object. For this, one has to evaluate the temporal phase difference at different instants. A quantitative measurement can be obtained after unwrapping the phase differences. Since the refractive index variations are encoded in the unwrapped phase, the use of the Gladstone-Dale relation allows determining density variations.

5.2. Proof of principle

The proposed method has been applied to the visualization and analysis of light bulb during its lighting. This bulb was submitted to a current to produce light and holograms were recorded at different instants after its lighting. **Figure 27** shows the recorded hologram when the bulb is off (a) and when the bulb is lighting (b). The speckle nature of the hologram is clearly observed. **Figure 27c** shows the amplitude image obtained with the discrete Fresnel transform. The stochastic screen and the ampoule can be clearly seen so that the strand of the bulb. **Figure 27d** and **e** shows respectively the modulo 2π digital fringes and unwrapped phase differences obtained between two instants (light off and light on). One can note a very large

http://dx.doi.org/10.5772/66111

amplitude variation since the phase values are in the range 10–50 rad (see the colour bar in **Figure 27e**). This measurement includes the contribution due to the refractive index change in the bulb and also a contribution due to the dilatation of the envelope and its refractive index variation due to the temperate increase inside the lamp (≈ 500°C). The 'numerical fringes' observed in **Figure 27d** exhibits the refractive index variations integrated in the glass container.

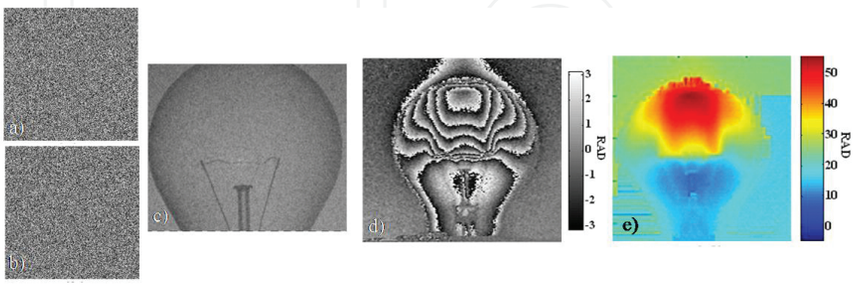

Figure 27. Quantitative measurement inside the bulb, (a) virtual phase extracted from numerical reconstruction (bulb off), (b) bulb lighting, (c) image amplitude of the strand, (d) modulo 2π phase computed from (a) and (b), (e) unwrapping of (d).

5.3. Comparison with silver-halide plate holographic interferometry

In order to check for the quality of the results obtained with the proposed method, the results obtained were compared with analogue image-holography [23]. The two possible set-ups are described in **Figure 28** and can be either transmission or reflection holographic interferometry. **Figure 28a** shows the transmission holography mode and **Figure 28b** that for reflection holography. Note that the set-ups require the use of photographic plates and that the diffuser is also used to get a stochastic screen to illuminate the object. The process is as follows: record a transmission or reflection hologram, apply the chemical treatment to the plate to develop and bleach, dry the plate, put the holographic plate in the set-up anew (exactly at the same location), at this step the holographic image of the ampoule is observable, adjust the camera lens to produce a focused image, then record real-time interferences between the initial bulb and that currently submitted to the current. Note that only the luminous intensity of interference fringes can be obtained, and not the phase image as it is the case for the digital holographic approach.

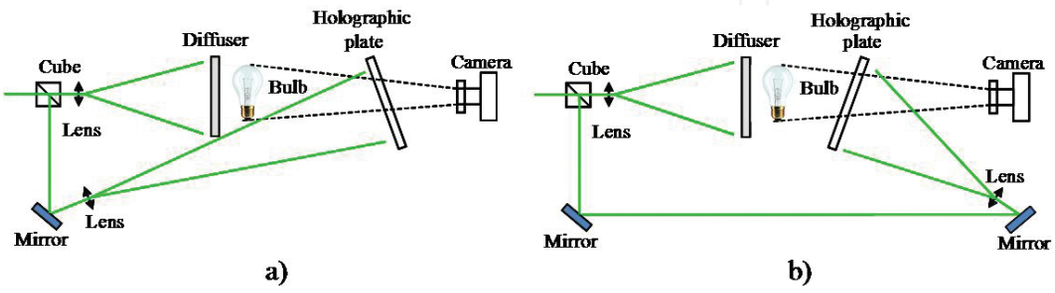

Figure 28. Image transmission holography (a) and image reflection holography (b).

Figure 29 shows a comparison between results obtained with digital holography and those obtained with image holography. **Figure 29a** shows the image obtained with the amplitude and phase change measured by digital holography, after calculating the intensity $I = A(1 + \cos(\Delta\varphi))$, where $\Delta\varphi$ is the phase change and A the amplitude image. **Figure 29b** shows the interference fringes obtained with the set-up of **Figures 28a** and **29c** shows those obtained with the set-up of **Figure 28b**. A very good agreement can be observed. Furthermore, the image quality given by each method can be appreciated. Image holography provides the best spatial resolution: the strand of the lamp can be clearly seen in **Figure 29b** and **c**. However, digital holography is more flexible since no chemical processing is required and a phase image can be obtained.

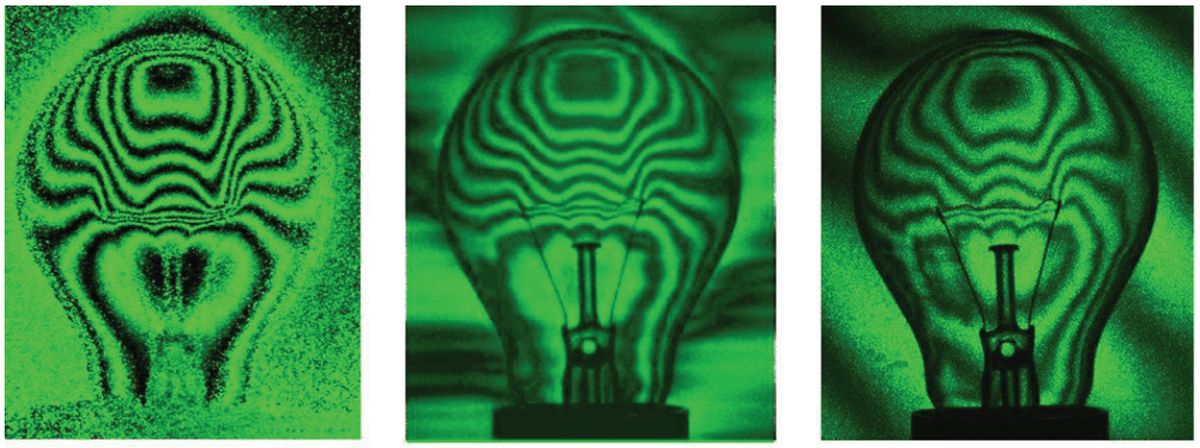

Figure 29. Comparison between intensity of fringes (a) fringes calculated with digital holography, (b) fringes obtained with transmission holography and (c) fringes obtained with reflection holography.

6. Conclusion

This chapter has shown several possibilities of digital holographic interferometry for analysing high-density gradients encountered in transonic and supersonic flows. Concerning the analysis of a small supersonic jet, a comparison is given between three different techniques, two techniques use reference waves: Michelson holographic interferometry and digital holography using Wollaston prisms; the last one uses a specific diffraction grating to obtain several different diffractions of measurement waves and to avoid having the reference wave.

For analysing transonic flows in wind tunnel, two types of interferometer have been developed. The first one is very simple to implement because it is a Michelson interferometer with double crossing of the test section for increasing the sensitivity and the second one is a Mach-Zehnder interferometer, more difficult to adjust, with a single crossing of the test section. These two interferometers are equipped with a pulsed laser and interferograms obtained have a very good quality and, basically, no phase shift.

Finally, a digital holographic method is proposed to visualize and measure refractive index variations, convection currents, or thermal gradients, occurring inside transparent but a strongly refracting object. The principle of this technique is provided through the visualization of refractive index variation inside a lighting ampoule. Comparisons with image transmission and reflection holographic interferometry demonstrate the high image and phase quality that can be extracted from the stochastic digital holographic set-up.

Currently, digital holographic interferometry is developed by ONERA for studying 3D flows from multi directional tomographic interferograms recorded in several directions. The aim is first to compare this method with other techniques yielding the gas density field as differential interferometry, back-oriented schlieren (BOS) and colour BOS; and secondly, to find the best compromise between the number of sight of view, the computation time and the results accuracy.

Acknowledgements

The authors thank the French National Agency for Research (ANR) for funding this work under grant agreement no. ANR-14-ASTR-0005-01.

Author details

Jean-Michel Desse* and François Olchewsky

*Address all correspondence to: Jean-Michel.Desse@onera.fr

ONERA, The French Aerospace Lab, Lille, France

References

[1] Katz J, Sheng J. Applications of holography in fluid mechanics and particle dynamics. Annu. Rev. Fluid Mech. 2010;42 p. 531–555.

[2] Atlan M, Gross M, Desbiolles P, Absil E, Tessier G, Coppey-Moisan M. Heterodyne holographic microscopy of gold particles. Opt. Lett. 2008;33(5) p. 500–502.

[3] Müller J, Kebbel V, Jüptner W. Characterization of spatial particle distributions in a spray-forming process using digital holography. Meas. Sci. Technol. 2004;15 p. 706–710.

[4] Sharma S, Sheoran G, Shakher C. Investigation of temperature and temperature profile in axi-symmetric flame of butane torch burner using digital holographic interferometry. Opt. Lasers Eng. 2012;50 p. 1436–1444.

[5] Dolocek R, Psota P, Ledl V, Vit T, Vaclavik J, Kopecky V. General temperature field measurement by digital holography. Appl. Opt. 2013;52(1) p. A319–A325.

[6] Demoli N, Vukicevic D, Torzynski M. Dynamic digital holographic interferometry with three wavelengths. Opt. Express. 2003;11(7) p. 767–774.

[7] Desse JM, Picart P, Tankam P. Digital Three-color holographic interferometry for flow analysis. Opt. Express. 2008;16(8) p. 5471–5480.

[8] Desse JM, Picart P, Tankam P. Digital three-color holographic interferometry applied to fluid and structural mechanics. Opt. Lasers Eng. 2012;50 p. 18–28.

[9] Goodman JW, Lawrence RW. Digital image formation from electronically detected holograms. Appl. Phys. Lett. 1967;11 p. 77–79.

[10] Picart P, Gross M, Marquet P. Basic fundamentals of digital holography. In: Picart P., editor. New Techniques in Digital Holography. ISTE Wiley, London; 2015 ISBN 978-1-84821-773-7.

[11] Desse JM, Picart P. Quasi-common path three-wavelength holographic interferometer based on Wollaston prisms. Opt. Lasers Eng. 2015;68 p. 188–193.

[12] Desse JM, Picart P, Olchewsky F. Quantitative phase imaging in flows with high resolution holographic diffraction grating. Opt. Express. 2015;23(18) p. 23726–23737.

[13] Gontier G, Carr P, Henon G. On differential interferometric device to arbitrarily rotate the fringes compared to the direction of the beams shift. Compt. Rend. Acad. Sci. 1966; 262 p. 674–677.

[14] Rodriguez O, Desse JM, Pruvost J. Interaction between a supersonic jet and a coaxial supersonic flow. Aerosp Sci Technol. 1997;11(6).

[15] Frankot RT, Chellappa R. A method for enforcing integrability in shape from shading algorithms. IEEE Trans. Pattern Anal. Mach. Intell. 1988;10(4) p. 439–451.

[16] Velghe S, Primot J, Guérineau N, Cohen M, Wattelier B. Wave-front reconstruction from multidirectional phase derivatives generated by multilateral shearing interferometers. Opt. Lett. 2005;30(3) p. 245–247.

[17] Kakue T, Yonesaka R, Tahara T, Awatsuji Y, Nishio K, Ura S, Kubota T, Matoba O. High-speed phase imaging by parallel phase-shifting digital holography. Opt. Lett. 2011;36(21) p. 4131–4133.

[18] Desse JM, Picart P. Stochastic digital holography for visualizing inside strongly refracting transparent objects. Appl. Opt. 2015;54(1) A1–A8.

[19] Schnars U, Kreis TM, Jüptner WO. Digital recording and numerical reconstruction of holograms: reduction of the spatial frequency spectrum. Opt. Eng. 1996;35 p. 977–982.

[20] Mundt J, Kreis T. Digital holographic recording and reconstruction of large scale objects for metrology and display. Opt. Eng. 2010;49 p. 125–801.

[21] Picart P, Leval J. General theoretical formulation of image formation in digital Fresnel holography. J Opt Soc Am A. 2008;25(7) p. 1744–1761.

[22] Li JC, Tankam P, Pen Z, Picart P. Digital holographic reconstruction of large objects using a convolution approach and adjustable magnification. Opt. Lett. 2009;34(5) p. 572–574.

[23] Desse JM, Tribillon JL. Real-time three-color reflection holographic interferometer. Appl. Opt. 2009;48(36) p. 6870–6877.

IntechOpen